nature materials

SUPPLEMENTARY INFORMATION

https://doi.org/10.1038/s41563-019-0336-1

Ultrafast generation and control of an electron vortex beam via chiral plasmonic near fields

G. M. Vanacore[1,10]*, G. Berruto[1,10], I. Madan[1], E. Pomarico[1], P. Biagioni[2], R. J. Lamb[3], D. McGrouther[3], O. Reinhardt[4], I. Kaminer[4], B. Barwick[5], H. Larocque[6], V. Grillo[7], E. Karimi[6], F. J. García de Abajo[8,9] and F. Carbone[1]

[1]Institute of Physics, Laboratory for Ultrafast Microscopy and Electron Scattering (LUMES), École Polytechnique Fédérale de Lausanne, Lausanne, Switzerland. [2]Dipartimento di Fisica, Politecnico di Milano, Milano, Italy. [3]SUPA, School of Physics and Astronomy, University of Glasgow, Glasgow, UK. [4]Faculty of Electrical Engineering and Solid State Institute, Technion, Haifa, Israel. [5]Ripon College, Ripon, WI, USA. [6]Department of Physics, University of Ottawa, Ottawa, Ontario, Canada. [7]CNR-Istituto Nanoscienze, Centro S3, Modena, Italy. [8]ICFO-Institut de Ciencies Fotoniques, The Barcelona Institute of Science and Technology, Castelldefels (Barcelona), Spain. [9]ICREA-Institució Catalana de Recerca i Estudis Avançats, Barcelona, Spain. [10]These authors contributed equally: G. M. Vanacore, G. Berruto. *e-mail: giovanni.vanacore@epfl.ch

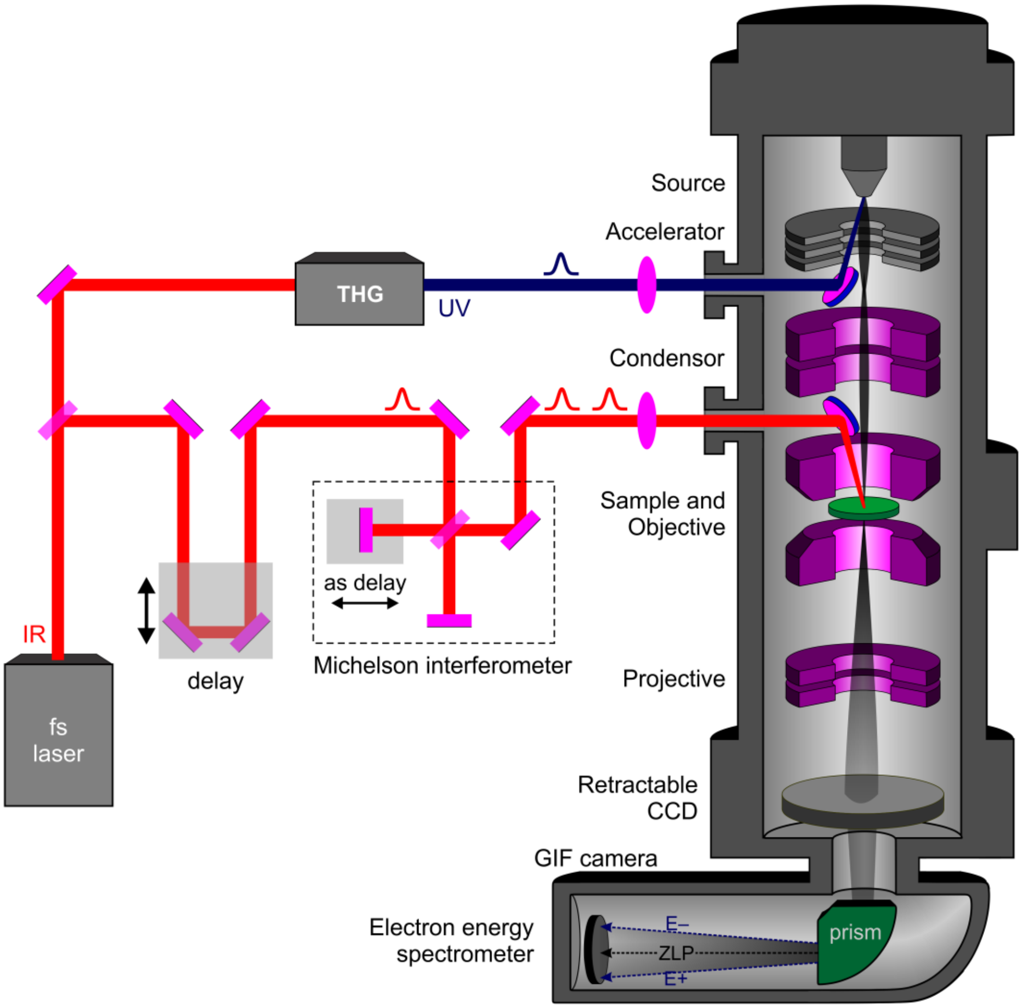

Figure S1. A schematic representation of the ultrafast transmission electron microscope used for the experiments presented in this Letter.

S1. Experimental detection of electron/chiral-plasmon interaction

A typical electron energy loss spectrum acquired in the region including and surrounding the nanofabricated hole is reported in Fig. S2, demonstrating multiple electron-plasmon energy exchanges experienced by the electron beam. The spectrum was taken with a ~ 1 eV Zero-Loss Peak (ZLP) for a sample orientation such that the interaction between the electron beam and the incident and reflected light beams vanishes while maintaining a significant electron-plasmon coupling (see section S2).

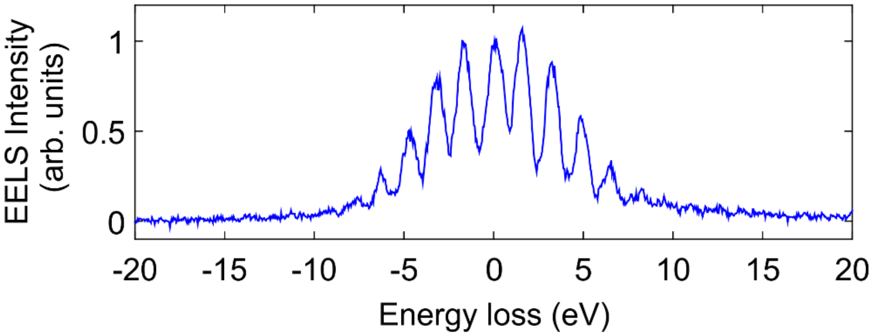

Figure S2. Representative electron energy-loss spectrum acquired in the region containing and surrounding the nanofabricated hole. Here, the angle α is equal to its critical value for vanishing electron-light interaction (only electron-plasmon interaction is present).

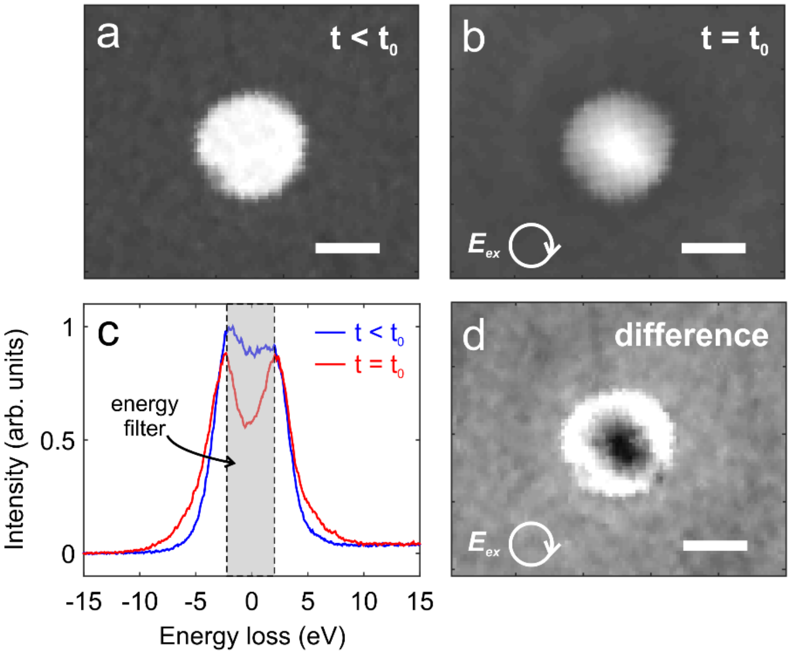

Figure S3. Experimental procedure used for the determination of the spatial distribution of the interaction strength within the hole. (a)-(b) Energy-filtered maps acquired before the arrival of the laser excitation pulse (panel a) and in coincidence with it (panel b). (c) Energy-filtering condition used for images in panels (a) and (b): a ~ 4 - 5 eV window was used to select electrons at the center of a ~ 6 - 8 eV Zero-Loss Peak (ZLP). (d) Spatial map of the interaction strength inside the hole obtained as the difference between the maps in (a) and in (b). In panels (a), (b) and (d) the scale bar is 0.5 µm.

Energy-filtered real-space images presented in the manuscript were acquired by selecting a ~ 4 - 5 eV window at the center of a ~ 6 - 8 eV Zero-Loss Peak (ZLP) (see Fig. S3c). This allowed us to monitor the depletion of the ZLP following the plasmonic excitation, and directly provided the spatial distribution of the inelastically-scattered electrons from the optically-excited plasmonic near fields. The data presented in Figs. 2a and 2f, which show an experimental measure of the interaction strength within the hole, are obtained by subtracting two energy-filtered images obtained with and without the pump laser excitation. This is shown in Fig. S3, for circularly-polarized light pumping.

S2. Analytical theory of electron-plasmon interaction

Upon transmission through the plasmon-supporting structure, the incident electron wave function $\psi_{\rm inc}(R,\phi,z,t)$ picks up inelastic components given by (1)

$$\psi_\ell(R,\phi,z,t)=\psi_{\rm inc}(R,\phi,z,t)\,J_\ell(2|\beta|)\,\exp\big(i\ell\arg\{-\beta\}+i\ell\omega(z/v-t)\big), \qquad \text{(S1)}$$

corresponding to an integer number ℓ of plasmons absorbed/emitted by a single electron (see also Eq. (1) of the main text). In Eq. (S1), R and ϕ are the radial distance and the azimuthal angle for a cylindrical reference frame centered at the hole, v represents the electron speed, and J_ℓ is the $\ell^{\rm th}$-order Bessel function of the first kind. The interaction between the electrons and the electromagnetic field is captured by the complex function $\beta(R,\phi)$, which can be written as

$$\beta(R,\phi)\approx\theta(R-R_{\rm hole})\left(A+B\left[\cos(\alpha_{\rm L})\cos(\phi)+\sin(\alpha_{\rm L})\,e^{i\delta_{\rm L}}\sin(\phi)\right]\frac{\exp(ik_{\rm SPP}R)}{\sqrt{k_{\rm SPP}R}}\right). \qquad \text{(S2)}$$

Here, $\alpha_{\rm L}$ and $\delta_{\rm L}$ are light polarization angles, $k_{\rm SPP}$ is the plasmon wave vector, $R_{\rm hole}$ is the hole radius, and the Heaviside function $\theta(R-R_{\rm hole})$ is present because we are describing here the interaction with the SPP in the film, outside the hole. The incident light is linearly polarized when $\alpha_{\rm L}$ is a multiple of $\pi/2$ (in particular, the polarization is in the plane determined by the electron and light beams for $\alpha_{\rm L}=0$), and elliptically polarized otherwise. The inelastic scattering of the electrons is mediated by the component of the electric field along the electron-beam direction, so we obtain analytical expressions for the position-independent coefficients A and B in Eq. (S2) by integrating the optical field along the electron trajectory, as described in detail below and in Refs. (1) and (2). We stress that both of these coefficients are proportional to the incident electric field amplitude $\mathcal{E}_0$.

Because of the finite angle $\delta=4.5°$ between the propagation directions of the laser and electron beams, we expect a nonzero A term, which describes the interaction of the electron beam with the incident and reflected light fields pertaining to the homogeneous part of the film. The remaining B term accounts for the interaction with the plasmon field scattered by the hole, which propagates with a complex in-plane wave vector $k_{\rm SPP}$ and exhibits an additional $1/\sqrt{R}$ decay as a function of the distance R from the center of the hole, characteristic of 2D radial plasmon waves.

Because the silver layer is thicker than the optical skin depth at the photon energy used in the experiment, and the TM reflection coefficient reduces to $r_{\rm TM} \approx e^{i\varphi_{\rm TM}}$ with $\varphi_{\rm TM} \approx 21^\circ$ at the photon energy under consideration, we find the following closed-form expression for the term A:

$$A = \frac{ev\mathcal{E}_0}{\hbar\omega^2}\,\cos(\alpha_{\rm L})\left[\frac{\sin\delta}{1-(v/c)\cos\delta} + \frac{e^{i\varphi_{\rm TM}}\sin(\delta-2\alpha)}{1+(v/c)\cos(\delta-2\alpha)}\right] \tag{S3}$$

where $v = 0.695\,c$ is the electron speed for the used acceleration voltage of 200 kV and c is the speed of light in vacuum. Incidentally, A can vary by an overall phase imposed by the temporal displacement of the electron wave function along the light optical period, so that it defines a global delay-controlled phase in β that only affects the relative phases of different ℓ components in Eq. (S1) and Eq. (1) of the main text. Also, we note that for a perfect mirror (i.e., $\varphi_{\rm TM} = 0$), the electron-light interaction vanishes (i.e., $A = 0$) when the tilt angle takes a critical value $\alpha = \alpha_{\rm C} = \tan^{-1}[\sin\delta\,/(\cos\delta - v/c)]$. If we consider the reflection phase $\varphi_{\rm TM}$ of the actual mirror, there is a small residual interaction due to the non-perfect reflectivity and the associated losses, and therefore β can only be minimized (but not eliminated) for a critical value of the angle α similar to the above value $\alpha_{\rm C}$.

The term B in Eq. (S2) accounts for the interaction with the plasmon field scattered by the hole, which propagates with a complex in-plane wave vector $k_{\rm SPP}$. A classical electromagnetic description of the Ag/Si_3N_4 film reveals two plasmon bands, which at the photon energy under consideration possess in-plane wavelengths $\lambda_{\rm SPP} = 2\pi/{\rm Re}\{k_{\rm SPP}\} \approx 708$ nm and 774 nm, and propagation distances $1/2{\rm Im}\{k_{\rm SPP}\}$ (for $1/e$ intensity decay) of 22.4 μm and 166 μm, respectively. We find experimentally that light-to-plasmon coupling through the hole, combined with electron-plasmon coupling through β, result in a dominant effect of the first of such plasmons, which has most of its associated energy density close to the Ag-Si_3N_4 interface. Further analysis reveals that $|B|^2 = \sigma_{\rm L-SP}/\sigma_0$, where $\sigma_{\rm L-SP}$ is the hole-radius-dependent light-to-plasmon coupling cross-section, while the parameter σ_0 only depends on the film composition and the layer thicknesses. For our samples and operation light frequency, we calculate $\sigma_0 \approx 3956$ nm^2 and 565 nm^2 for the 708-nm and 774-nm plasmons, respectively, which additionally confirms a more efficient electron-plasmon coupling for the Ag-Si_3N_4 plasmon.

From Eq. (S2), we find that for circular or elliptical light polarization, the phase of the interaction strength β evolves nearly linearly with ϕ (i.e., $\arg\{\beta\} \propto \phi$). This is shown in Fig. S4 under the same conditions adopted in the experiments. Consequently, we conclude that the factor $\exp(i\ell\arg\{-\beta\})$ in Eq. (S1) and in Eq. (1) of the main text translates into an overall corkscrew phase factor $\exp(\pm i\ell\phi)$ in the electron wave function ψ_ℓ, which therefore carries an OAM $\pm\ell\hbar$.

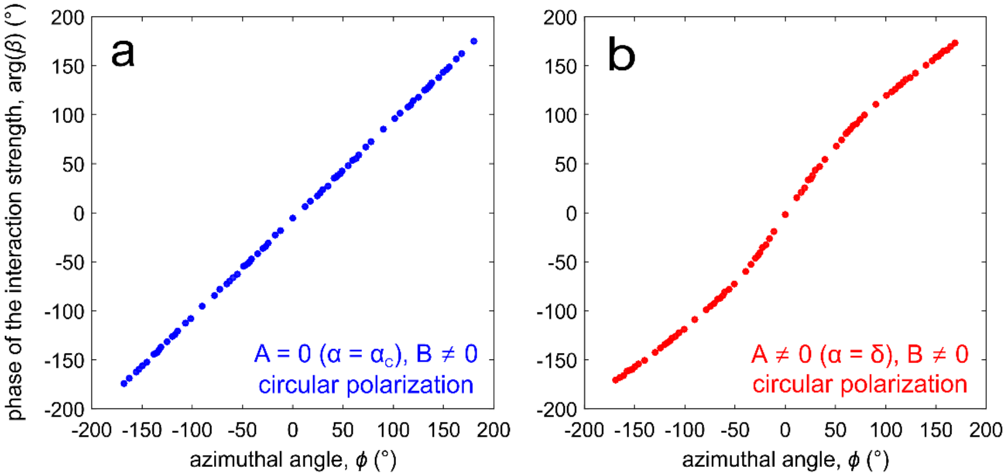

Figure S4. Calculated phase of the interaction strength, $\arg\{\beta\}$, as a function of the azimuthal angle ϕ for two different conditions: (a) $A = 0$ $(\alpha = \alpha_C)$, $B \neq 0$; and (b) $A \neq 0$ $(\alpha = \delta)$, $B \neq 0$ (with $A \ll B$), where A and B represent the terms in Eq (S2) describing the electron-light and electron-plasmon interactions, respectively.

Direct comparison between theory and experiment is obtained for the real-space electron distribution, which is readily provided by the expression of ψ_ℓ in Eq. (S1) for the selected PINEM sidebands ℓ according to the experimentally adopted energy window:

$$I(R,\phi) = \sum_\ell |\psi_\ell|^2 \tag{S4}$$

The analytical results obtained following the theory developed in this section for the adopted experimental conditions (see section S1) are reported in Fig. 1d in the main text and agree well with the experimental observations shown in Fig 1c. The best agreement is obtained using fitting parameters $|B|^2 \approx 2.5$ and $arg\{B\} \approx -107°$. In our imaging method, where we use an experimental energy window of ~ 4 - 5 eV around the point at zero-energy-loss peak, the main contribution to the signal is determined by the plasmon-induced depletion of the ZLP $(\ell = 0)$; the lateral sidebands $(\ell \neq 0)$, which all have the same spatial distribution and come from the same plasmon resonance, produce only a minor contribution to the contrast in the image of the radiated SPP. To show this, we performed additional simulations. In Fig. S5 we plot the calculated inelastically-scattered maps obtained by averaging the electron signal over three different energy intervals around the zero-energy loss: 1 eV (left), 4 eV (center), and 7.2 eV (right). It can be clearly observed that the pattern remains the same in terms of spatial periodicity, phase distribution and chirality. The only difference is a small change in the peak-to-valley contrast, which nevertheless we believe to be inconsequential for the present work. This would only matter if one would like to quantitatively extract the generated near-field directly from the data, which is not the focus of the current paper. The central panel in Fig. S5, which best corresponds to the experimental conditions of Fig. 1c, is the one represented in Fig. 1d.

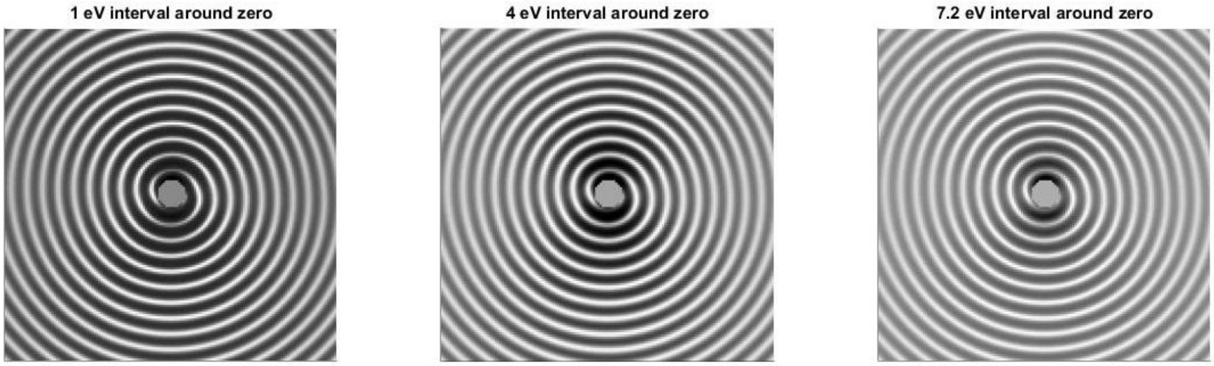

Figure S5. Inelastically-scattered maps obtained by averaging the electron signal over three different energy intervals around the zero-energy loss: 1 eV (left), 4 eV (center), and 7.2 eV (right).

As mentioned earlier in this section, the analytical expression adopted for β in Eq. (S2) is only valid for the region outside the hole, and that is why the central opening is omitted in the analytically-calculated inelastically-scattered electron maps. Nevertheless, we can theoretically obtain the field distribution inside the hole using FDTD numerical simulations as shown in the main text and detailed in section S3 below.

The same formalism can also be applied to simulate the coherent control experiments shown in Fig. 4 of the main text. In this case, two phase-locked light pulses are used to finely control the relative phase of the optically-excited plasmons by varying their relative delay Δt in fractions of the optical cycle. The calculated inelastic real-space maps for two elliptically polarized light pulses with parallel and perpendicular major axes are shown in Figs. S6 and S7, respectively, together with the calculated coherent modulation of intensity, spatial periodicity, and helicity of the chiral plasmonic pattern.

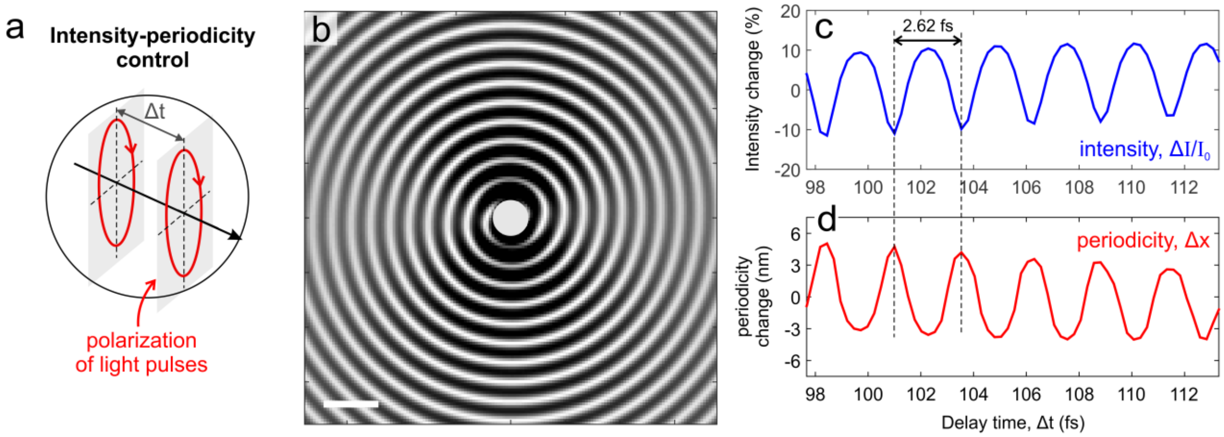

Figure S6. (a) Two phase-locked elliptically polarized light pulses with parallel major axes and delayed by Δt are used to coherently launch two interfering chiral SPPs at the edge of the hole. (b) Calculated real space map of inelastically-scattered electrons for $\Delta t = 98$ fs (scale bar is 2 μm). (c)-(d) Calculated coherent modulation of the intensity (panel **c**) and of the spatial periodicity (panel d) of the plasmonic fringes with a temporal period of ~ 2.6 fs, obtained by varying the delay time Δt. The large delay between the two ~ 50 fs-pulses makes the direct optical interference negligible (see also Ref. 1), and thus only the interference between SPPs is relevant.

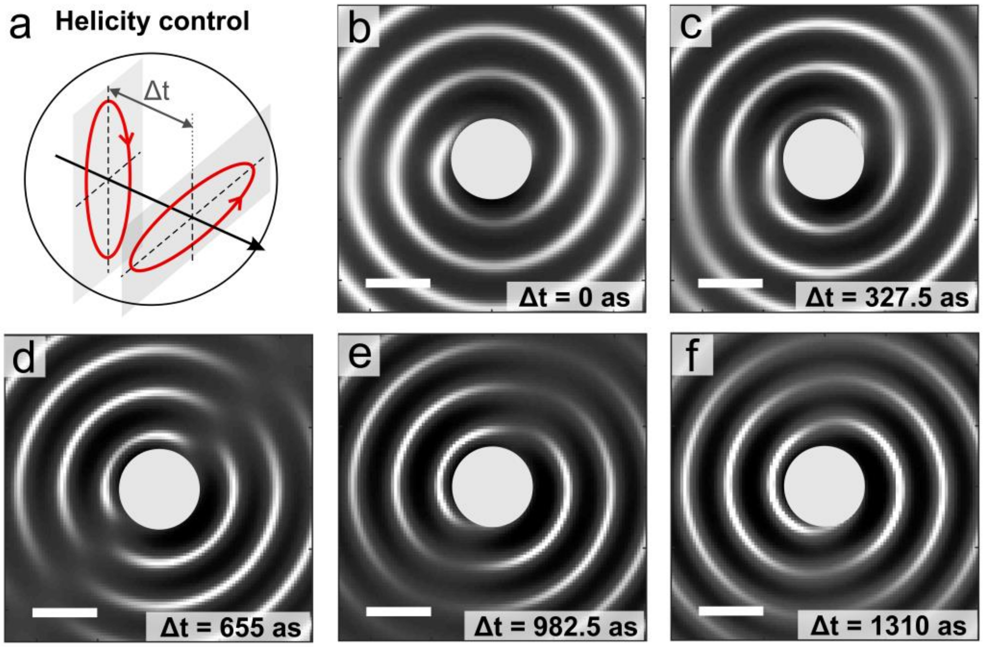

Figure S7. (a) Two phase-locked elliptically polarized light pulses with perpendicular major axes and delayed by Δt are used to coherently launch two interfering chiral SPPs at the edge of the hole. (b)-(f) Calculated real space maps of inelastically-scattered electrons for different delay times Δt varied in steps of 327.5 as (the scale bar is 1 μm). In this configuration, the helicity of the plasmonic field is observed to switch from counter-clockwise to clockwise within an optical cycle.

S3. Finite-difference time-domain (FDTD) simulations and numerical determination of $\boldsymbol{\beta}$

Three-dimensional finite-difference time-domain (FDTD) simulations are performed with a commercial software (3). The refractive index of Si_3N_4 is set to *n* = 2, while the experimental dielectric constant of silver is taken from the literature (4). The source is a weakly focused, elliptically or circularly-polarized Gaussian beam reproducing the illumination conditions of the experiments. The mesh size inside and around the hole is about 7 nm. Perfectly matched layers are used as boundary conditions, with a simulation area as wide as 45x45 μm^2 in the x-y plane and ± 2 μm in the z direction, to minimize artifacts possibly created by residual spurious boundary reflections.

In Fig. S8a we report the simulations of the real part of the z component of the electric field, $\mathrm{Re}\{\mathcal{E}_z\}$, plotted on the *x-z* plane, when considering a circularly polarized incident light. The electric field $\mathcal{E}_z$ is maximum at the edge of the hole and rapidly decreases when moving away from it. From the simulated maps, it is also possible to numerically determine the interaction strength β by invoking its original definition (1):

$$\beta(R,\phi) = \frac{e}{\hbar\omega}\int_{-\infty}^{\infty} dz\,\mathcal{E}_z(R,\phi)\exp\left(-\frac{i\omega z}{v}\right) \tag{S5}$$

The results are reported in Fig. S8b, which shows the absolute value of the calculated β plotted as a function of the radial coordinate R (this result is independent of the choice of ϕ). The figure clearly shows that the modulation of the electron wave function after interaction with the specimen is dominated by the coupling to the optical near field at the hole, which imprints its chirality onto the electron beam.

Using the FDTD method we have simulated the spatial distribution of the interaction strength β both inside and outside the hole for two light polarization states, circular and linear (see Figs. 2b and 2g for the modulus, and Figs. 2d and 2i for the phase). The simulations reproduce well the experimental data, where a zero-field region with cylindrical- or mirror-symmetry is visible inside the hole when circularly- or linearly-polarized light is used, respectively. It is worth noting that the electron distribution inside the hole associated with different sidebands ℓ can have slightly different spatial profiles, as one can observe in the space-energy maps shown in Figs. 2e and 2j. However, they all exhibit the same symmetry: cylindrical or mirror, depending on the light polarization. This is the relevant information that we discuss in the manuscript, and small deviations of the measured profile from the purely inelastic distribution goes beyond the scope and focus of this work on ultrafast vortex beams.

In order to investigate the scalability of the proposed approach to subwavelength plasmonic structures, we have performed additional FDTD simulations of the optical field and the corresponding interaction strength β *via* Eq. (S5) as a function of hole diameter. The results are presented in Figure S9 below, where we are considering a Ag layer with a thickness of 40 nm under illumination with light at 800 nm wavelength. A clear resonance is visible for a diameter of ~ 200 nm. These results show that scalability to subwavelength plasmonic structures is indeed not only possible but also desirable. Resonances with even smaller hole diameters could in principle be reached using a proper choice of light wavelength and metallic layer thickness.

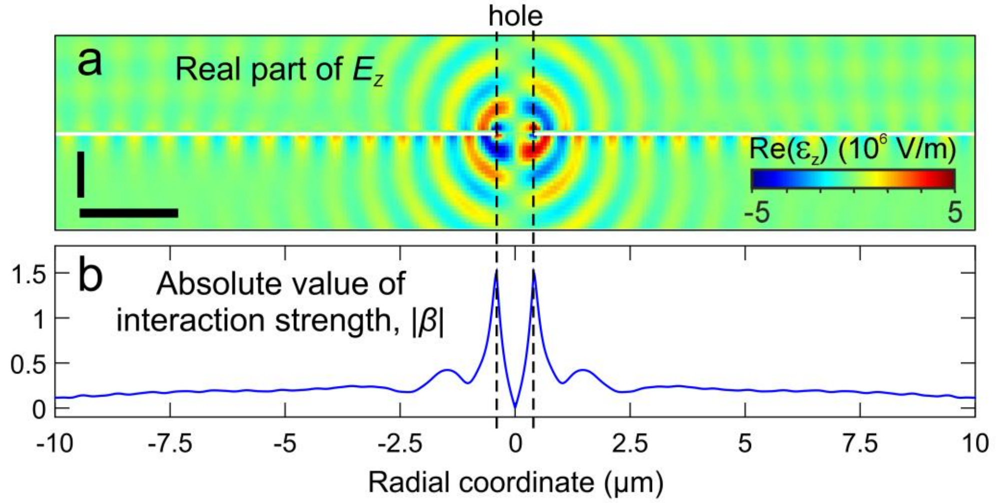

Figure S8. (a) The results of FDTD simulation demonstrating the real part of the z component of the electric field , $\mathrm{Re}\{\mathcal{E}_z\}$, plotted in the x-z plane, when considering a circularly polarized incident light (the horizontal scale bar is 2 μm whereas the vertical scale bar is 1 μm). (b) The calculated absolute value of the interaction strength β plotted as a function of the radial coordinate R for a given azimuthal angle ϕ, extracted from the FDTD simulations shown in panel a using Eq. (S5).

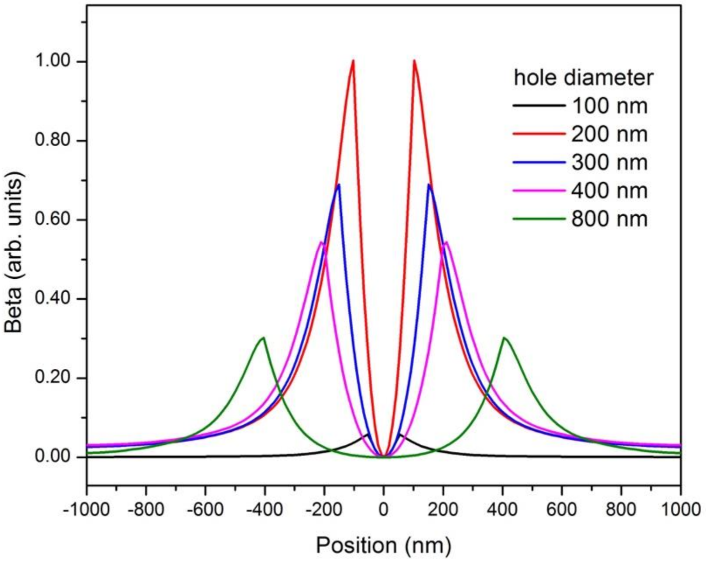

Figure S9. Simulations of the interaction strength $|\beta|$ as a function of hole diameter for illumination with light of 800 nm wavelength. The thickness of the Ag layer is 40 nm.

S4. Electron vortex beam calculations

Further insights into the results demonstrated in Fig. 2 of the main text can be also retrieved by employing a standard simulation tool commonly adopted in TEM studies (5). To simulate the effect of the chiral near-field on the electron wave function, we consider a spatially-confined spiral phase plate of order ℓ whose extension is determined by the hole diameter (~ 800 nm) (see Fig. S10b for the case $\ell = 1$). The far-field amplitude of the momentum-resolved electron wave function $\Psi_\ell(k_x, k_y)$ is thus calculated as the Fourier transform of this distribution, which is basically a top-hat function with a corkscrew phase factor $\exp(\pm i\ell\phi)$. The result is a hypergeometric Gaussian beam sampled in the far-field. The total Fourier-plane intensity is then obtained as $I_F(k_x, k_y) = \sum_{|\ell|=0}^{+\infty} w_\ell \left|\Psi_\ell(k_x, k_y)\right|^2$, where the weights w_ℓ are extracted from the experimentally measured energy spectrum (see Fig. S2). In the absence of interaction, this calculation readily provides a nearly-Gaussian distribution in momentum space (Fig. S10a), whereas the interaction with the spatially-limited phase singularity modifies the transverse profile creating a doughnut-shaped probability distribution (Fig. S10c-d). The latter is the typical signature of a vortex beam, so this simplified model correctly reproduces our experimental observations and the theoretical calculations presented in the main text.

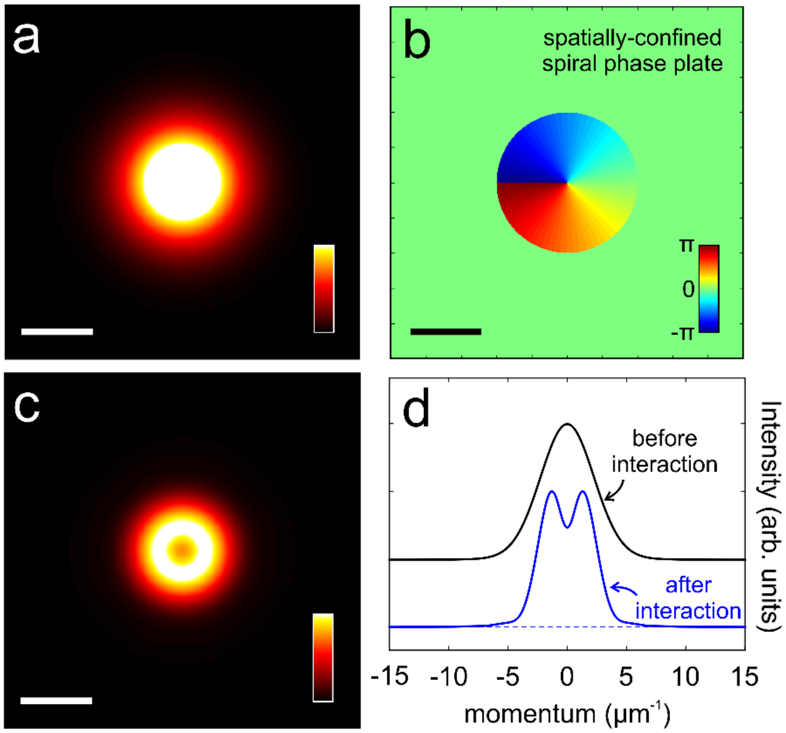

Figure S10. (a) Calculated reciprocal-space intensity distribution of a plane-wave electron beam (scale bar is 4 μm^{-1}). (b) Spatially-confined phase singularity of order $\ell = 1$ with an extension determined by the hole diameter (the scale bar is 400 nm). (c) Calculated reciprocal-space electron intensity distribution obtained from the interaction of a plane wave with a spatially-limited phase singularity similar to the one shown in panel (b), using the STEM CELL software tool (5) (the scale bar is 4 μm^{-1}). The final map is obtained by incoherently summing the contributions of all ℓ's with weights determined by the electron spectrum shown in Fig. S2. (d) Line profiles across the central part of the far-field images reported in panels (a) and (c).

We conclude this section by presenting a simple estimate of the amplitude of the doughnut signal in the experimentally measured reciprocal-space maps, giving the net contribution of electrons with nonzero OAM. In our high-dispersion-diffraction experiments we use a micrometer circular aperture placed in close proximity to the image plane and centered around the hole. This procedure, together with the low electron transmissivity through the continuous metal film surrounding the hole, guarantees that a significant portion of the electrons reaching the detector at small diffraction angles has indeed interacted with the chiral field in the hole.

These considerations allow us to estimate the contribution to the dip in the far field image due to interaction with the chiral near field through the following formula $\eta_0\, A_{\rm h}/\big(A_{\rm h}+T(1-\eta_1)(A_{\rm ap}-A_{\rm h})\big)$, where the parameters are directly derived from our experiments. In particular, the numerator represents the electrons having acquired a nonzero OAM and hence creating a doughnut profile, while the denominator refers to the electrons in the direct beam at $k\approx 0$. Also, $A_{\rm h}=0.8^2\pi/4\ \mu{\rm m}^2$ is the hole area, $A_{\rm ap}=15^2\pi/4\ \mu{\rm m}^2$ is the total aperture area, $T=0.013$ is the transmissivity through the specimen away from the hole, $\eta_0\sim 0.9$ is the fraction of electrons interacting with the chiral near field in the hole, and $\eta_1\sim 0.58$ is the probability for an electron crossing the thick region to interact with the SPPs radiated from the hole (i.e., we discount electrons that undergo scattering at high angles). The result gives a doughnut contribution of 0.33 ± 0.12 of the total beam height, which is compatible with both our measurements and calculations (see Fig. 3 in the main text).

S5. Parton density function of an OAM-carrying proton

In a given reference framework, a proton characterized by a certain momentum can be decomposed into collinearly moving partons (quark and gluons) (6), each of which carries a fraction η of the total momentum of the proton. To such partons we can attribute a generalized parton distribution function (GPD), $H_q(\eta,\chi)$, which describes how a parton q exchanges momentum upon collisions, where χ is proportional to the absolute square of the momentum transfer. To provide concrete information on the internal structure of the particle, GPDs can be related to other quantities. One of these consists of an impact-parameter-dependent parton density function (PDF) of the particle, $f(\eta,\mathbf{r})$, where $\mathbf{r}$ represents the transverse spatial coordinates. The function $f(\eta, \mathbf{r})$ can for instance be related to the transverse charge density of the proton $\rho(r)$ using the relation (7)

$$\rho(r) \equiv \sum_q e_q \int d\eta\, f(\eta, \mathbf{r}), \tag{S6}$$

where $r = |\mathbf{r}|$ and e_q corresponds to the charge attributed to the parton q. For localized protons, $f(\eta, \mathbf{r})$ approximately corresponds to the Fourier transform of the GPD (40). However, this relation does not necessarily hold for a proton defined by a transverse wave function Ψ. In such cases, the Fourier transform $\mathcal{F}_\Psi$ of an impact-parameter-dependent PDF, defined by a transverse wavepacket Ψ, becomes (8)

$$\mathcal{F}_\Psi(\eta, \mathbf{r}) = N \int d\mathbf{p}\, \Psi^*(\mathbf{p}')\Psi(\mathbf{p}) H_q(\eta, q^2), \tag{S7}$$

where N is a normalization constant.

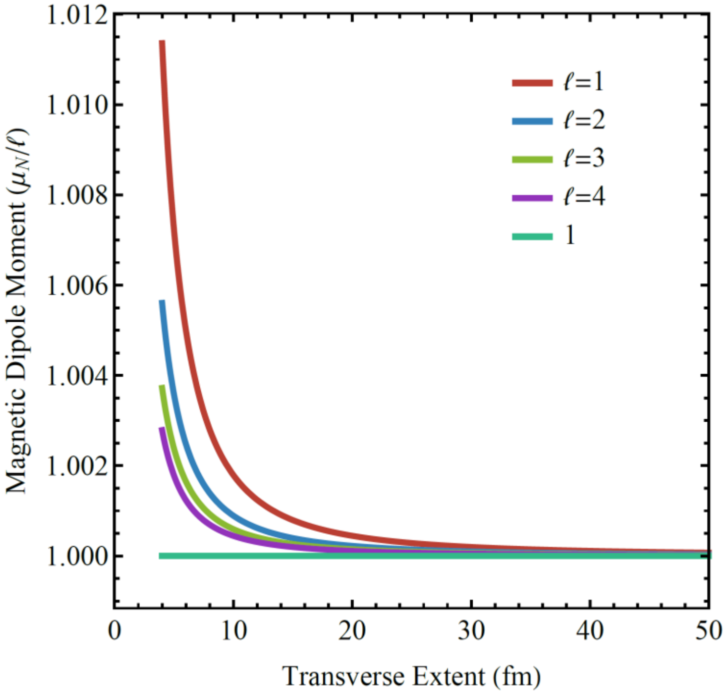

Figure S11. Magnetic dipole moment of OAM-carrying protons. Semi-classically calculated magnetic dipole moments of protons carrying ℓ units of OAM. This quantity is shown in units of the nuclear magneton (μ_N) for proton wave functions characterized by different transverse extents.

Though formally correct, the above charge density can be estimated by means of a semi-classical approach treating it as a convolution of the particle's probability density function and known measures of its internal charge density. For mathematical convenience, the latter is approximated as a sum of Gaussian functions of various widths whose integral adds up to the particle's charge. A similar approach can be used to approximate the particle's current density by means of a convolution between the particle's probability current density and its internal charge density. These wave function-dependent quantities can thereafter be used to estimate some of the particle's properties by means of classical multipole expansions. For instance, as shown in Fig. S11, the described theory has been used to calculate how the internal structure of an OAM-carrying proton affects its magnetic dipole moment. To account for the presence of OAM in the proton's wave function, the latter were modeled by means of OAM-carrying Laguerre-Gauss modes.

References

1. G. M. Vanacore et al., Nat. Commun. **9**, 2694 (2018).
2. F. J. García de Abajo, B. Barwick, and F. Carbone, Phys. Rev. B **94**, 041404(R) (2016).
3. FDTD Solutions, Lumerical Inc., Release 2017a.
4. P. B. Johnson and R. W. Christy, Phys. Rev. B **6**, 4370 (1972).
5. V. Grillo, E Rotunno, STEM_CELL: a software tool for electron microscopy. Part I Simulations, Ultramicroscopy **125**, 97-111 (2012).
6. E. B. Manoukian , Quantum Field Theory I: Foundations and Abelian and Non-Abelian Gauge Theories. Springer International Publishing, 13 Dec 2016
7. G. A. Miller, Phys. Rev. Lett. **99**, 112001 (2007).
8. M. Burkardt, Phys. Rev. D **62**, 071503 (2000).